

Anisotropy and Stress Dependence of Permeability in the Barnett Shale

Athma R. Bhandari · Peter B. Flemings · Peter J. Polito ·
Michael B. Cronin · Steven L. Bryant

Received: 30 July 2014 / Accepted: 28 February 2015 / Published online: 8 March 2015
© Springer Science+Business Media Dordrecht 2015

Abstract We document vertical permeability of $2.3 \times 10^{-21} \text{ m}^2$ (2.3 nd) and horizontal permeability of $9.5 \times 10^{-20} \text{ m}^2$ (96.3 nd) in two Barnett Shale samples. The samples are composed predominantly of quartz, calcite, and clay; have a porosity and a total organic content of $\sim 4\%$ each; and have a thermal maturity of 1.9 % vitrinite reflectance. Both samples exhibit stress-dependent permeability when the confining pressure is increased from 10.3 to 41.4 MPa. We measure a permeability anisotropy, the ratio of the horizontal to the vertical permeability, of ~ 40 . We find that the permeability anisotropy does not vary with effective stress. Multiscale permeability, as demonstrated by pressure dissipation, is related to millimeter-scale stratigraphic variation. We attribute the permeability anisotropy to preferential flow along more permeable layers and attribute the stress dependence to pore closure. A determination of permeability anisotropy allows us to understand flow properties in horizontal and vertical directions and assists our understanding of upscaling. Characterization of stress dependency allows us to predict permeability evolution during production.

Keywords Mudrocks · Pulse-decay permeability · Anisotropy · Stress dependence · Heterogeneity

Electronic supplementary material The online version of this article (doi:[10.1007/s11242-015-0482-0](https://doi.org/10.1007/s11242-015-0482-0)) contains supplementary material, which is available to authorized users.

Steven L. Bryant was formerly in Department of Petroleum and Geosystems Engineering, Cockrell School of Engineering, The University of Texas at Austin, Austin, Texas, USA.

A. R. Bhandari (✉) · P. J. Polito
Bureau of Economic Geology, Jackson School of Geosciences, The University of Texas at Austin,
Austin, TX, USA
e-mail: athma.bhandari@beg.utexas.edu

P. B. Flemings · M. B. Cronin
Jackson School of Geosciences, The University of Texas at Austin, Austin, TX, USA

S. L. Bryant
Schulich School of Engineering, University of Calgary, Calgary, Canada

List of symbols

α	Pressure-sensitivity factor (Pa^{-1})
μ	Gas viscosity (Pa s)
ϕ	Porosity of core plug
a	Ratio of sample pore volume to volume of upstream reservoir
b	Ratio of sample pore volume to volume of downstream reservoir
b_k	Klinkenberg's gas slippage factor (Pa)
c	Gas compressibility (Pa^{-1})
s	Semilog slope of the differential pressure decay (at 90% decay)
$f(a, b)$	$(a + b + ab) - (1/3)(a + b + 0.4132ab)^2 + 0.0744(a + b + 0.0578ab)^3$
k_a	Apparent gas permeability (m^2)
k_0	Apparent gas permeability at $P_c - P_p = 0$ (m^2)
k_∞	Absolute (Klinkenberg's corrected) permeability
k_h	Horizontal permeability (m^2)
k_v	Vertical permeability (m^2)
L	Length of core plug (m)
P	Pressure in sample (Pa)
P_1	Upstream reservoir pressure (Pa)
P_2	Downstream reservoir pressure (Pa)
P_c	Confining pressure (Pa)
P_D	Dimensionless pressure
P_p	Average pore pressure (Pa)
ΔP	Differential (upstream – downstream) pressure at time t (Pa)
ΔP_0	Initial differential pressure (Pa)
t	Time elapsed (s)
x	Distance along the sample (m)

1 Introduction

Hydrocarbons produced from mudrocks (gas or oil shales) are proving to be a remarkable worldwide energy resource (EIA 2013). Hydraulic fracturing and horizontal drilling are being used to increase production rates from these reservoirs (Waters et al. 2009). The broad conceptual view is that hydrocarbons migrate relatively short distances through the matrix to fracture networks that are induced by hydraulic fracturing (Stegent et al. 2011). The induced fracture network may also enhance existing natural fracture networks in the rocks (Gale et al. 2007), further shortening the distance through the matrix that hydrocarbons must travel to access a fracture. This conceptual view has been quantified through reservoir simulators (Bustin and Bustin 2012; Clarkson et al. 2012; Clarkson 2013; Hinkley et al. 2013) and analytical models (Silin and Kneafsey 2011; Patzek et al. 2013). At the simplest level, a dual-scale permeability model has been envisioned, where the effective permeability is controlled by the fracture spacing and the matrix permeability (Patzek et al. 2013).

While there is broad acceptance of the concept that fractures and matrix together play a role in transporting hydrocarbons from the formation to the well bore, the details of these processes remain poorly understood. For example, very long timescale production data in these low-permeability systems are required to evaluate the relative contribution of fracture-versus-matrix-dominated flow. Patzek et al. (2013) suggest that the production data in the Barnett Shale record the interaction of two hydraulically induced fractures in horizontal

wells over a timescale of 5–10 years. They show that a matrix permeability on the order of 50 nd ($\sim 5.0 \times 10^{-20} \text{ m}^2$) with a fracture spacing of 100 m will interfere in 50 years, whereas if the matrix is 500 nd ($\sim 5.0 \times 10^{-19} \text{ m}^2$), the interaction will occur in 5 years. These values of matrix permeability required are 20- to 200-fold larger than the values of a few nanodarcsies found for shale core samples in the laboratory experiments. In turn, production timescales are so long that it is difficult to investigate the evolution of rock properties (for example, how compressibility and permeability vary with overburden stress and pore pressure). The contribution of the matrix to the bulk permeability of shale reservoirs declines during drawdown and pore-pressure depletion because of increasing overburden stress, which can have significant implications on well performance and on production data analysis and forecasting.

An alternative approach to understanding matrix permeability is to study intact samples at the laboratory scale. However, this is also challenging. First, because of the long testing times in low-permeability material (below 10^{-18} m^2), a well-designed and well-constructed apparatus must be used to minimize leaks in the pore fluid lines; precisely control temperature; and accurately measure and control fluid pressure, volume, and flow. Often the transient pulse-decay technique (Brace et al. 1968; Hsieh et al. 1981; Dicker and Smits 1988; Jones 1997) is used to measure permeability relatively rapidly. Second, intact samples are necessary. Mudrocks in particular exhibit bedding-parallel weaknesses, and sampling disturbance (e.g., coring) can easily introduce microfractures along the bedding planes (Gale and Holder 2010). Any fractures present will dominate the flow behavior, and thus, matrix permeability cannot be properly characterized.

Despite the challenges, there is a growing body of literature on the topic of matrix permeability. Published permeability values vary by several orders of magnitude and depend on the applied effective stress (the difference between confining and pore pressure) and the orientation of bedding relative to flow direction (parallel or normal to bedding). Vermylen (2011), Heller (2013), and Heller et al. (2014) report permeability values ranging between 10^{-17} and 10^{-21} m^2 for multiple shale samples, including the Mississippian Barnett Shale. In Scandinavian Alum and Toarcian Posidonia Shales, Ghanizadeh et al. (2014a, b) report permeabilities between 10^{-17} and 10^{-22} m^2 . Measurements on Devonian gas shale samples by Soeder (1988) observed stress-dependent permeability behavior and demonstrate that the presence of any petroleum as a mobile liquid phase in the pores significantly reduces the gas porosity and permeability. In Devonian gas shales, Chalmers et al. (2012) report a reduction in permeability of over five orders of magnitude, with a 15 MPa increase in effective stress. Bustin et al. (2008) measured permeability in multiple shale samples, including the Mississippian Barnett Shale, and found a decrease in permeability of two to three orders of magnitude as effective stress is increased from 6.9 to 24.1 MPa. In Western Canadian and Woodford Shales, Pathi (2008) identified permeability anisotropy (difference between horizontal and vertical permeability) of three to four orders of magnitude. In Devonian and Ordovician shale samples, Tinni et al. (2012) found permeability anisotropy of ~ 100 and a permeability decrease in one to three orders of magnitude, with an increase in effective stress to 34.5 MPa. Metwally and Sondergeld (2011) found permeability anisotropy of ~ 3 –5 only in gas shales. A key conclusion we can draw from previous matrix permeability studies is that it is difficult to find a definite answer regarding the primary controls of permeability and regarding permeability anisotropy and stress dependence.

Here, we present a laboratory study on gas flow within centimeter-scale low-permeability mudrock samples. We characterize two Barnett Shale cores—a vertical plug (flow perpendicular to bedding) and a horizontal plug (flow parallel to bedding)—with respect to microstructure, mineralogy, total organic content (TOC), and thermal maturity. We use the

pulse-decay technique and measure gas permeability over a range of effective stresses by holding pore pressure constant and varying confining pressure. We interpret vertical permeability of $2.3 \times 10^{-21} \text{ m}^2$ (2.3 nd) and horizontal permeability of $9.5 \times 10^{-20} \text{ m}^2$ (96.3 nd) at 3.5 MPa effective stress. Vertical and horizontal permeability decrease from 2.3×10^{-21} to $5.4 \times 10^{-22} \text{ m}^2$ and 9.5×10^{-20} to $2.1 \times 10^{-20} \text{ m}^2$, respectively, when the effective stress is increased from 3.5 to 35.0 MPa, which yields a permeability anisotropy value of ~ 40 . We show that there is multiscale permeability behavior in these cm-scale rocks.

2 Sample Description and Characterization

We extracted two intact core plugs for permeability measurements (vertical plug 2V and horizontal plug 6H1; Fig. 1a, b), from $\sim 2330 \text{ m}$ depth in the Mitchell Energy T.P. Sims #2 well

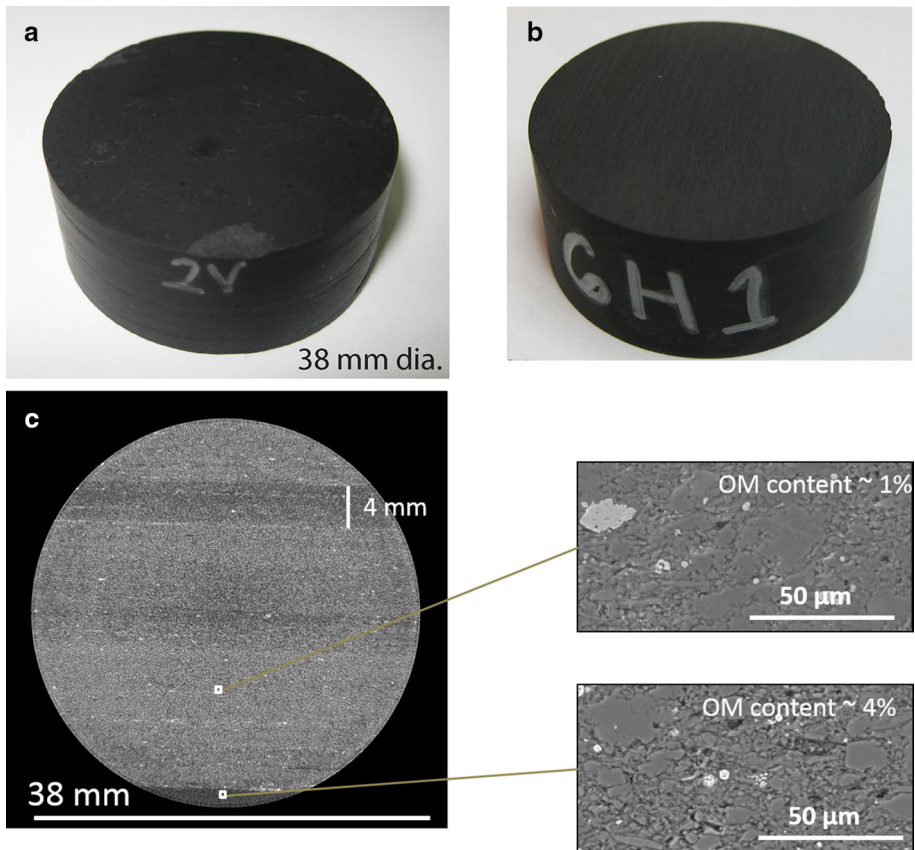


Fig. 1 a, b Photographs of test core plugs 2V and 6H1. Plug 2V is extracted normal to the bedding plane and Plug 6H1 is extracted parallel to the bedding plane. c CT image of core plug 6H1. The CT image voxel size is $\sim 40 \mu\text{m}$. No visible microfractures are present. Bedding of 4–8 mm is obvious; the darker regions contain materials of lower density, and the lighter regions indicate materials of higher density. Scanning electron images taken of polished thin section yielded $\sim 1\%$ organic matter (OM) content in the lighter layers and $\sim 4\%$ OM content in the darker layers

in the Mississippian Barnett Formation (Loucks and Ruppel 2007). Cores from this well are stored at the Core Research Center, Bureau of Economic Geology, at The University of Texas at AustinTM. The Barnett Formation is composed of fine-grained [clay-size (<2 μm) to silt-size (<62.5 μm)] particles (Loucks and Ruppel 2007). There are three common lithofacies present in the Barnett: laminated siliceous mudstone, laminated argillaceous lime mudstone (marl), and skeletal argillaceous lime packstones (Hickey and Henk 2007; Loucks and Ruppel 2007). Hickey and Henk (2007) provide a detailed study of local lithofacies and physical stratigraphy of the lithological section where 2V and 6H1 originated. We extracted core plugs with a thin-wall diamond coring bit, using tap water for coolant. We trimmed each plug with a low-speed/low-friction saw and polished each end with 220-grit (average particle diameter = 68 μm) sandpaper. We heated the core plugs to 60 °C to drive off any free fluid present until we achieved a constant mass (within 0.01 g).

We used microscale X-ray computed tomography (μ-CT) to view the full diameter of the core plugs and to assess internal disturbances (Fig. 1c). CT highlights density differences across the sample. The available resolution (~40 μm) is insufficient to observe organic matter and pore-scale features (pores in both inorganic and organic matter and their types) and to pick up microfractures that could control flow (permeability as high as $1.3 \times 10^{-10} \text{ m}^2$). However, it is adequate to identify microfractures (>40 μm), nodules, and bedding features (mm-scale variation). Using μ-CT, we observe that the plug 2V is largely homogenous (not shown), while images of 6H1 reveal mm-scale layering (Fig. 1c).

We prepared thin sections for low-magnification (~2200×) grain fabric analysis under the scanning electron microscope (Fig. 2a, b). The samples are dominated by silt-sized fragments (between 10 and 35 μm) (Fig. 2a, b). The horizontal image (Fig. 2a) appears isotropic with no preferential alignment, whereas the vertical image (Fig. 2b) shows elongated grains preferentially oriented horizontally. We prepared 1-cm cube samples for high-magnification (>40,000×) imaging of nanopores, using an Ar-ion-beam milling technique (Loucks et al. 2009). The silt-sized fragments (light gray) are surrounded by organic material (darker gray) pockmarked with smaller pores (Fig. 2c, d). Loucks et al. (2012) describe these irregular, bubble-like, elliptical pores as intraparticle organic-matter pores. The pore diameters range from a few nanometers up to several hundred nanometers. Barnett Shale is therefore a natural nanoporous material, with the only porosity we observe being within the organic material and with little to no intergranular porosity. These observations are consistent with previous microstructural studies (Loucks et al. 2009; Chalmers et al. 2012; Curtis et al. 2012).

End trimmings of the vertical and horizontal plugs have a TOC of 3.9 and 3.8 %, respectively, and a thermal maturity of 1.9 % Ro (Table 1), with the type IV kerogen indicating a high level of maturation. The TOC and thermal maturity of our samples are in close agreement with the Barnett samples studied by Loucks et al. (2009). Our analysis of the bulk composition using X-ray powder diffraction (XRPD) shows that both samples are predominantly composed of quartz, calcite, and clay minerals (Table 2).

3 Pulse-Decay Permeability Experiments and Experimental Setup

We conducted permeability measurements using the transient pulse decay method (Brace et al. 1968; Jones 1997). In this method, the sample is hydraulically connected to upstream and downstream reservoirs. Initially, the pore pressure in the sample is maintained at equilibrium with the upstream and downstream reservoir pressures. We then increase pressure in the upstream reservoir with a pulse of gas on the order of 10 % of the initial pore pressure. We next allow the system to re-equilibrate. We record the upstream and downstream pressures

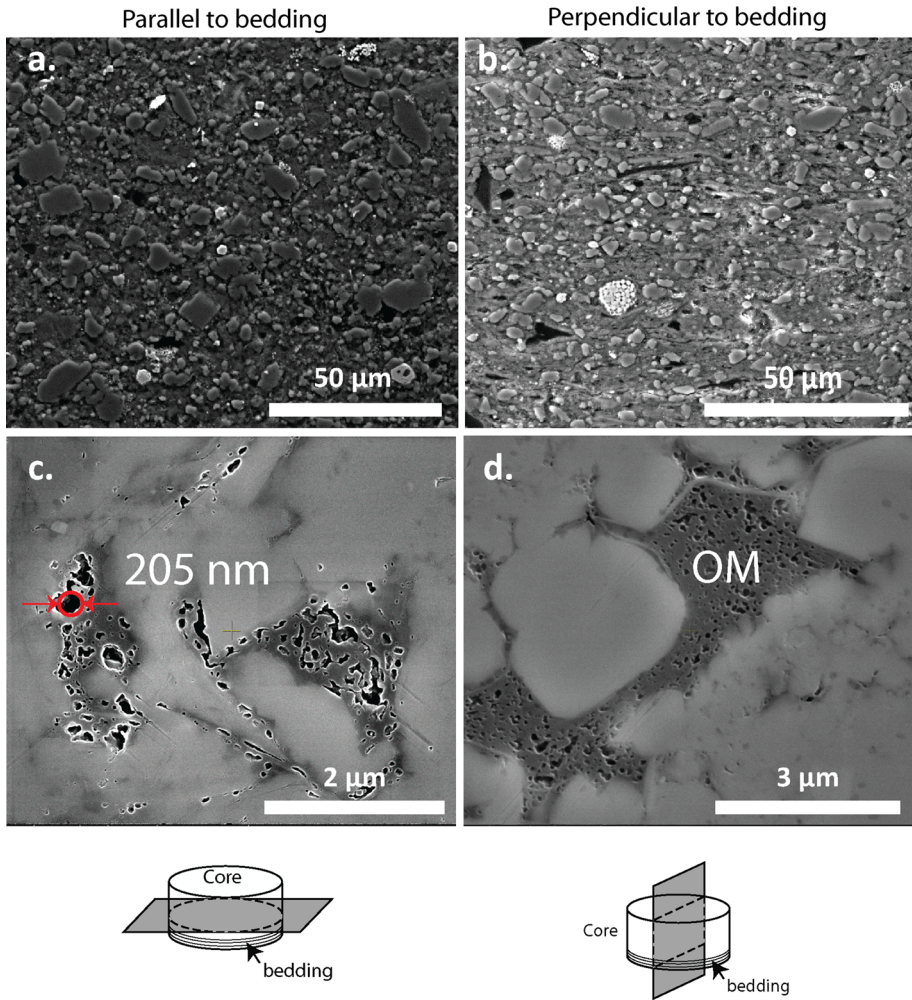


Fig. 2 Horizontal (a, c) and vertical (b, d) images taken parallel and perpendicular to bedding. **a, b** Backscattered electron images taken from thin sections. **c, d** Backscattered electron images taken from argon-ion-milled samples. Isotropic (a) and anisotropic (b) grain fabric within the Barnett Shale. Note a preferred orientation of particles parallel to the bedding; the bedding is *horizontal*. High-resolution images (c, d) show that pores are predominantly in OM. *Black areas* are OM. Pore size ranges from a few nanometers to 200 nm

Table 1 Summary of TOC and maturity analyses^a

Sample	Leco TOC (wt% HC)	Percent Carbonate (wt%)	Rock-Eval S1 (mg HC/g)	Rock-Eval S2 (mg HC/g)	Rock-Eval S3 (mg CO ₂ /g)	T_{\max} (°C)
2	3.90	22.80	0.52	0.82	0.44	503
6	3.77	25.62	–	–	–	–

S1: free oil content; S2: remaining generation potential; S3: organic carbon dioxide yield

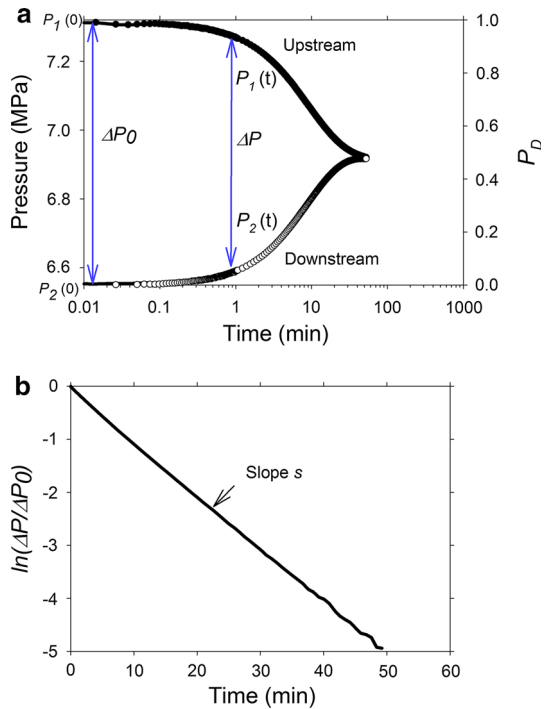
^a Geomark Research Limited carried out these analyses using Rock-Eval methods

Table 2 Summary of XRPD analyses^a

Sample	Minerals								
	Quartz (%)	Plagio-clase (%)	Calcite (%)	Dolomite (%)	Pyrite (%)	Musco-vite (%)	Illite plus illite-smectite (%)	Other (%)	Total (%)
2	32.3	2.4	7.0	5.4	2.5	3.8	39.8	0.8	99.9
6	43.1	2.9	5.4	22.7	2.0	5.7	17.1	1.1	100

^a Macaulay Scientific Consulting Limited analyzed our samples using standard XRPD methods

Fig. 3 Principle of the transient pulse-decay test. **a** Initially, the system is under equilibrium at a pore pressure of 6.55 MPa ($P_2(0)$). Then, a pressure pulse of ~690 kPa is applied in the upstream reservoir. The pressure then dissipates slowly into the sample pore volume and the downstream reservoir volume. The vertical axis (right) is the dimensionless pressure P_D with a range of 0 to 1. $P_D(\text{upstream}) = (P_1(0) - P_1(t)) / (P_1(0) - P_2(0))$ and $P_D(\text{downstream}) = (P_2(t) - P_2(0)) / (P_1(0) - P_2(0))$. **b** Differential pressure (upstream pressure/downstream pressure) versus time plot indicating the exponential decay



until they converge (Fig. 3a) and use the slope of differential pressure versus time to interpret permeability (Fig. 3b).

The core plug is enclosed in a 75-durometer Viton sleeve, which is mounted in a hydrostatic pressure cell (Fig. 4). We used argon gas (molecular diameter = 0.38 nm) as the pore fluid and vacuum pump oil as the confining fluid. In all our tests, the initial equilibrium pore pressure was at 6.55 MPa (950 psia). After allowing the sample to remain at the initial pore pressure for ~96 h, we closed valves 1 and 3 (Fig. 4), separating the core plug and the downstream reservoir by the upstream reservoir and pumps, and increased the upstream reservoir pressure by ~0.69 MPa (~100 psi). We shut valve 2, separating the upstream reservoir from the pump. We then opened valve 1 to start the permeability test. The elevated pressure on the upstream reservoir drives the flow of gas through the core to the downstream reservoir. The differential pressure decays exponentially with time (Fig. 3b), and we can then interpret the permeability using the late-time slope at 90 % decay, i.e., corresponding to a value of $\ln(\Delta P / \Delta P_0) =$

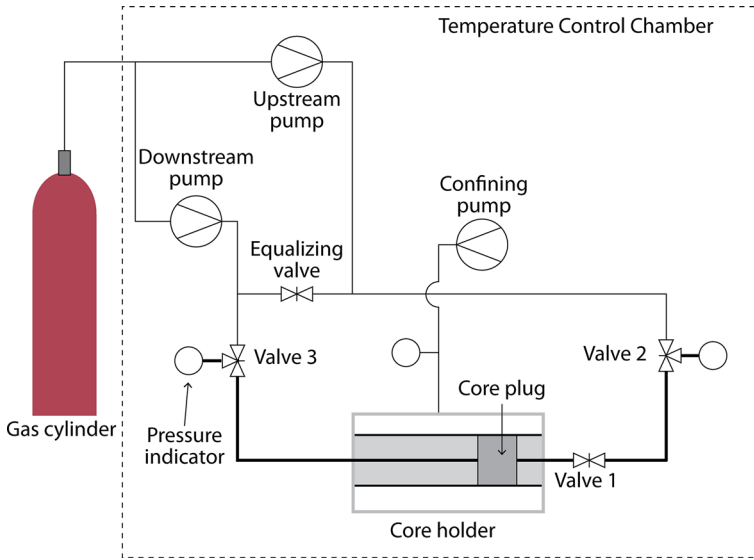


Fig. 4 Schematic diagram for the experimental setup. The setup consists of two pore-pressure pumps, one confining-pressure pump, a core holder, plumbing lines with valve fittings, and temperature control and data acquisition systems. The temperature of the setup is maintained at $30 \pm 0.05 \text{ }^\circ\text{C}$ during the tests. We used Quizix Q5000 (10 kpsia maximum pressure) pumps to control the pore pressure in the upstream and downstream sides and a Quizix QX pump to control the confining pressure. We used two absolute pressure transducers [maximum range = 35 MPa (5000 psi); accuracy = 0.04% FS] to measure pore pressures in the upstream and downstream reservoirs and one pressure transducer (maximum range = 69 MPa; accuracy = 0.04% FS) to measure confining pressure. We logged the temperature and pressure readings with National Instrument’s LabVIEW. The volumes of upstream and downstream reservoirs (including valves, transducers, and fittings) were calibrated from gas expansion tests using steel billets of known pore volumes and a steel blank as described by Ning (1992)

–2.303. The slope stabilized (becomes linear, Fig. 3b) after ~20% decay, indicating single-exponential behavior (Dicker and Smits 1988).

The differential equation describing the gas pressure inside the sample, $P(x, t)$, as a function of distance along the sample (x) and time (t), is given by

$$\frac{\partial^2 P}{\partial x^2} = \frac{c\mu\phi}{k} \frac{\partial P}{\partial t} \quad \text{for } 0 < x < L \quad \text{and } t > 0 \tag{1}$$

with initial and boundary conditions:

$$P(x, 0) = P_2(0) \quad \text{for } 0 < x < L \tag{2}$$

$$P(0, t) = P_1(t) \tag{3}$$

$$P(L, t) = P_2(t) \quad \text{for } t \geq 0 \tag{4}$$

Parameters are defined in the nomenclature table. Equation (1) follows from conservation of mass and Darcy’s law. We assumed that the matrix is homogeneous with a single porosity (ϕ) and the quantities c, μ, k are pressure dependent. In our tests, we kept the pressure pulse small (~10% of the initial pore pressure); therefore, the pore pressure variations are negligible across the sample, which allow us to assume c and μ are constant. Because our pore fluid is gas, the compressibility of equipment and sample (bulk and its mineral constituents) can be ignored compared to the gas compressibility (c). If we had used a liquid

Table 3 Sample dimensions and reservoir volumes

	Sample 2V	Sample 6H1
Diameter (mm)	37.81 ± 0.06	37.85 ± 0.06
Length (mm)	16.30 ± 0.04	17.64 ± 0.04
Upstream volume (ml)	1.96 ± 0.08	2.120 ± 0.052
Downstream volume (ml)	2.26 ± 0.09	1.763 ± 0.067

pore fluid, c would be an effective compressibility (Dicker and Smits 1988; Hsieh et al. 1981). Equation (2) indicates that at the start of the experiment the pressure in the sample is equal to the downstream reservoir pressure. Equations (3) and (4) state that the upstream and downstream faces of the sample are in contact with their respective adjacent reservoirs. Table 3 summarizes the sample dimensions and the reservoir volumes for our experiments.

The full analytical solution of Eq. (1) is given by Hsieh et al. (1981). A simple analytical expression to estimate permeability (Eq. 5) from the measured decay curve (Fig. 3b) is given by Dicker and Smits (1988). They show that this expression is valid (accurate within 0.3 %) as long as the pore volume is not greater than the volumes of the upstream and downstream reservoirs (this is true for our experimental design).

$$k = \frac{c\mu\phi L^2 s}{f(a, b)} \quad (5)$$

We used the average pore pressure in the sample, taken as the final equilibrium pressure reached, to estimate c and μ using NIST data (NIST 2014). We compared the analytical estimate of permeability obtained by using Eq. (5) with the estimate of permeability obtained by solving Eq. (1) numerically, using a finite-difference scheme; the difference between these estimates is <1 %.

In this study, since we used gas for permeability measurements, the permeability estimated using Eq. 5 is influenced by the gas slippage effect (Klinkenberg 1941). Our estimated values are therefore apparent gas permeability. We will discuss in Sect. 5.1 possible deviations of these values from the equivalent liquid permeability estimated using the correlation given by Heid et al. (1950). Since we used argon gas, we neglected the effects of adsorption (Cui et al. 2009).

4 Experimental Results

We measured porosity using both helium (on whole plugs and crushed samples) and mercury (on proximally located chips), with the helium porosity being three to four times higher in both plugs 2V and 6H1 (Table 4). This suggests that not all pore space is accessed by the mercury at 413.7 MPa (60,000 psi) maximum injection pressure, which corresponds to ~3.6 nm pore throat. We used the helium porosity values measured in whole core plugs for the ϕ value (Eq. 5) to calculate permeability. We emphasize that the pulse-decay permeability calculated using Eq. (5) is not a strong function of porosity.

We also used the GRI crushed-rock method to interpret permeability (Table 5). It is not possible to apply confining stress using this method; therefore, measurements are essentially at zero effective stress. Details of this method are given by Luffel et al. (1993). The GRI permeability for sample from core 2 is $\sim 9.8 \times 10^{-20} \text{ m}^2$ (99.6 nd) and for sample from core 6 is $\sim 3.6 \times 10^{-20} \text{ m}^2$ (36.3 nd).

Table 4 Porosities using helium porosimeter method, GRI crushed-rock method, and MIP

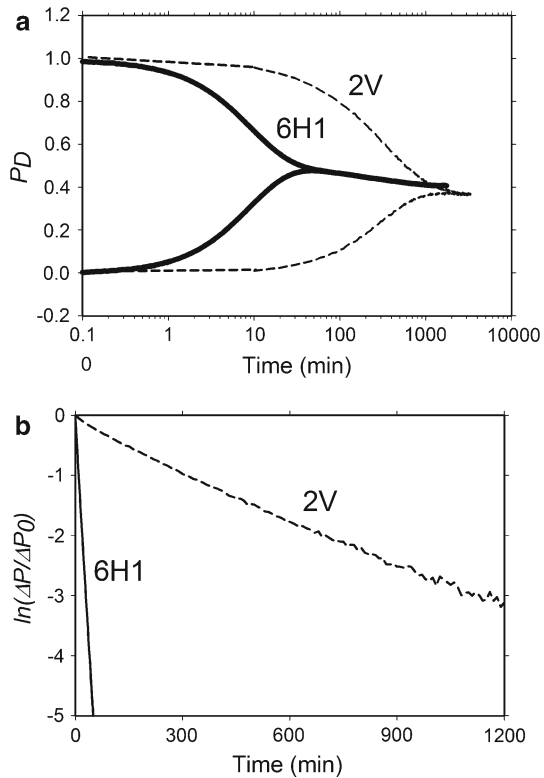
Sample	Porosity using helium porosimeter method ^a	Dry helium porosity using GRI crushed-rock method ^b	Porosity using MIP ^c
	% of bulk volume	% of bulk volume	% of bulk volume
2	3.9 ± 1.0 (2V)	5.9	1.2
6	4.1 ± 1.0 (6H1)	4.9	1.2

^a Measured in-house using Boyle’s law gas expansion principle in whole core plug reported as the mean ± 1 standard deviation. The bulk volume was calculated by geometry (Table 3)

^b Analyzed by Weatherford Ltd. (these values also shown in Table 5)

^c Analyzed by Porotechnology using Mercury Injection Porosimetry (MIP). We used the correction approach of Comisky et al. (2011) which specifically accounts for the pore volume compression of the sample before mercury has been injected into the largest set of interconnected pores

Fig. 5 **a** Pulse-decay data for vertical (2V) and horizontal (6H1) core plugs. The confining pressure is 10.3 MPa and the pore pressure is 6.9 MPa. The timescale of experiment is ~30 h for 2V and <1 h for 6H1. **b** Differential pressure versus time plots for 2V and 6H1. A steeper negative slope corresponds to higher permeability. Using Eq. (5), we get $k_v = 2.3 \times 10^{-21} \text{m}^2$ (for core plug 2V) and $k_h = 9.5 \times 10^{-20} \text{m}^2$ (for core plug 6H1). This gives a permeability anisotropy ratio of $k_h/k_v \sim 40$



The differential pressure (ΔP_0) of ~0.69 MPa (~100 psi) dissipated in <1h for the horizontal sample 6H1 (solid line, Fig. 5, where P_D is dimensionless pressure). In contrast, the differential pressure dissipated in 30 h for the vertical sample 2V (dashed line, Fig. 5). Based on Eq. (5), the permeabilities of core plugs 2V and 6H1 are $2.3 \times 10^{-21} \text{m}^2$ (2.3 nd) and $9.5 \times 10^{-20} \text{m}^2$ (96.3 nd), respectively, at an effective stress of 3.5 MPa. Permeability

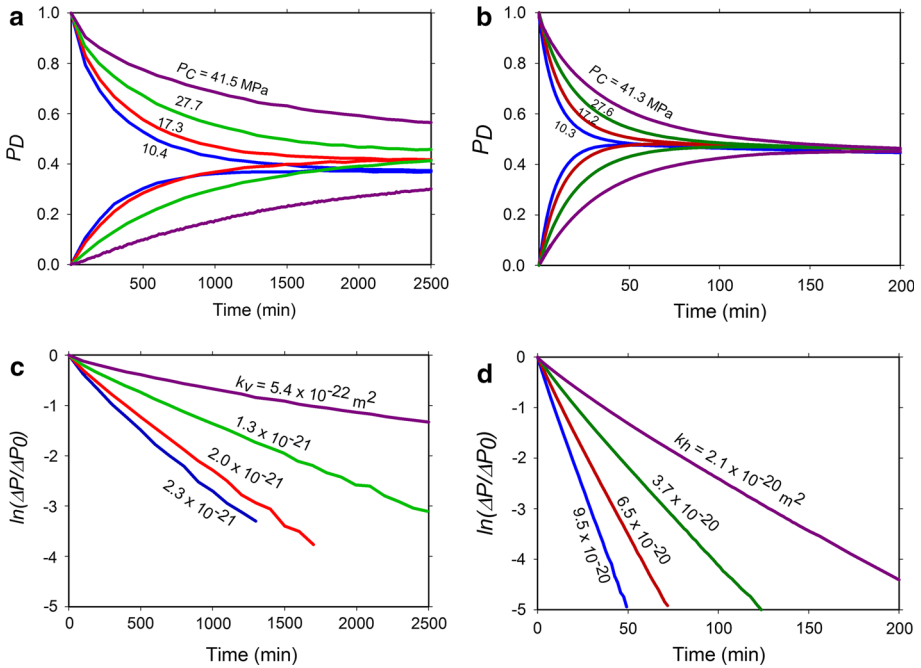


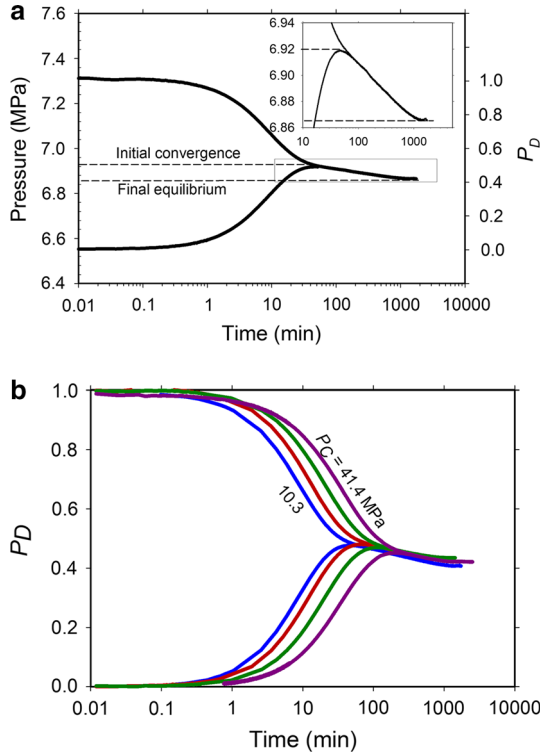
Fig. 6 Plots of dimensionless reservoir pressure versus time for core plugs 2V (a) and 6H1 (b) at confining pressures of 10.3, 17.2, 27.6, and 41.4 MPa. In all tests, the pore pressure is kept at ~6.9 MPa. Differential pressure declines more rapidly at lower confining pressures, which yields a steeper slope in the corresponding plots of differential pressure versus time (c, d). This implies that permeability decreases with increasing confining pressure. Between each test stage, we increased/decreased the confining pressure at a rate of approximately 172.4 kPa/min. We allowed the system to equilibrate for ~4 days after each change in confining pressure

anisotropy, the ratio of the horizontal to vertical permeability, is 38.7 at 3.5 MPa effective stress.

The pulse-decay time (as shown in the horizontal axis) increases gradually as confining pressure is increased from 10.3 to 17.2, 27.6, and 41.4 MPa for both samples (Fig. 6a, b). This behavior is further demonstrated by the decreasing slope of the differential pressure curves with the increasing confining pressure (Fig. 6c, d). Permeabilities of core plug 2V and 6H1 decreased from 2.3×10^{-21} to $5.4 \times 10^{-22} \text{m}^2$ and from 9.5×10^{-20} to $2.1 \times 10^{-20} \text{m}^2$, respectively (Fig. 6c, d). The permeability anisotropy, however, remained constant at ~40 for all effective stresses. The pressure-sensitivity factors α , defined as in $k = k_0 \exp(-\alpha(P_c - P_p))$ (Best and Katsube 1995), of both samples in this study are $0.0435 \text{ (MPa}^{-1})$ (The online version contains supplementary data files given as text document).

Figure 7a shows over 30 h of pressure-time behavior in core plug 6H1 at an effective stress of 3.5 MPa. In this particular test, we maintained a constant confining pressure of 10.3 MPa and equilibrium (initial) pore pressure of 6.6 MPa; the background leak rate was ~1.8 kPa/h and the pressure-time data were leak-corrected. Initially, the upstream and downstream pressures converge (“initial convergence”) after ~50 min. We then observed a secondary decline in both the upstream and downstream pressures. The pressure dissipation initially started at a rate of 12.5 kPa/h and gradually slowed down and reached the background leak rate of 1.8 kPa/h in ~30 h (“final equilibrium”). This behavior persisted at higher effective stresses;

Fig. 7 **a** Pressure dissipation at two timescales on core plug 6H1: initial convergence and then a slow overall dissipation at late time resulting in the secondary decline—characteristics of multiscale behavior (Kamath et al. 1992; Ning et al. 1993). **b** This two timescale behavior persists at higher confining pressure conditions



however, the time for initial convergence increased from approximately 60 to 300 min as effective stress is increased from 3.5 to 35 MPa (Fig. 7b).

This dual-time-scale pressure dissipation behavior is characteristic of multiscale permeability behavior (Kamath et al. 1992; Ning et al. 1993). We believe that this multiscale behavior is due to stratigraphic layering (Fig. 1c), which results in permeability contrast between layers. Assuming the initial flow is only through the more permeable layers, we estimate using pressure data almost half of the total porosity ($\sim 6\%$) resides in these layers. The upstream and downstream pressures initially equilibrated through these more permeable layers, followed by pressure dissipation into less permeable layers. The permeability of these high- and low-permeability layers can be estimated by analyzing the observed transients before and after the initial convergence pressure. In this study, however, we determined the permeability assuming homogeneous sample and using only the pressure-time data collected before the initial convergence pressure (first transient) for all effective stresses.

5 Discussion

5.1 Horizontal and Vertical Permeability Values

We interpret vertical permeability of $\sim 2.3 \times 10^{-21} \text{ m}^2$ (2.3 nd) and horizontal permeability of $\sim 9.5 \times 10^{-20} \text{ m}^2$ (96.3 nd) at 3.5 MPa effective stress in two Barnett Shale samples. Our horizontal permeability (sample 6H1, squares, Fig. 8) is similar to that measured by Kang

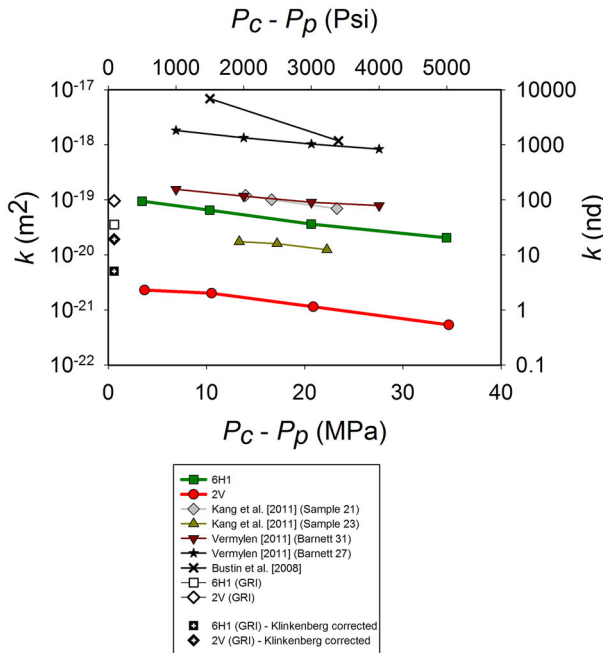


Fig. 8 Permeability versus effective confining pressure for both plugs. Our horizontal permeability measurements are within a range similar to those presented in the literature for intact Barnett samples [1.6×10^{-19} to $6.0 \times 10^{-20} m^2$ (Vermilyen 2011); 1.3×10^{-19} to $1.0 \times 10^{-20} m^2$ (Kang et al. 2011)]. The permeability using the crushed-rock GRI method, in which it is not possible to take into account the stress effects and directional permeability dependencies, for samples from core 2 and core 6 are Klinkenberg-uncorrected $9.8 \times 10^{-20} m^2$ (diamond) and $3.6 \times 10^{-20} m^2$ (square), and Klinkenberg-corrected $1.9 \times 10^{-20} m^2$ (filled diamond, cross-haired) and $5.1 \times 10^{-21} m^2$ (filled square, cross-haired), respectively. The permeability anisotropy persists at higher confining pressures. The probable error (uncertainty) for our permeability measurement is ~ 0.5 nd

et al. (2011) samples 21 and 23 and by Vermilyen (2011) sample Barnett 31. Vermilyen (2011) sample Barnett 27 (stars, Fig. 8), which was an interbedded carbonate layer surrounded by organic shale matrix, had a permeability $10\times$ greater than our horizontal permeability. The aforementioned studies measured permeability in the horizontal direction; thus, we are only able to directly compare our more permeable sample.

The GRI permeability for core 2 is $9.8 \times 10^{-20} m^2$ (99.6 nd) and for core 6 is $\sim 3.6 \times 10^{-20} m^2$ (36.3 nd) (Table 5; Fig. 8, respectively). Since these GRI measurements were conducted at a much lower gas pressure (0.7–1.4 MPa or 100–200 psi) than our pulse-decay permeability measurements at 6.9 MPa pore pressure, the Klinkenberg effect (Klinkenberg 1941) becomes physically more significant. To approximately take this effect into account for comparing our pulse decay with GRI measurements, we used the correlation given by Heid et al. (1950) to calculate the Klinkenberg’s gas slippage factor b_k using our measured permeability as an input for the liquid permeability (Table 6). Various correlations are available in the literature (Jones and Owens 1979; Ziarani and Aguilera 2012). The data used in Heid et al. (1950) correlation are from oil-field cores with permeability values between $\sim 10^{-12} m^2$ and $\sim 10^{-17} m^2$ for air at 25 °C. b_k is a function of the porous medium, the gas, and the temperature; it increases with decreasing permeability. We then use the Klinkenberg (1941) expression: $k_a = k_\infty \left(1 + \frac{b_k}{P_p} \right)$, which relates the apparent gas permeability k_a

Table 5 Results of permeability using GRI crushed-rock method^a

Sample	As-received bulk density (gm/cc)	Dry bulk density (gm/cc)	Dry grain density (gm/cc)	Dry helium porosity (% of bulk volume)	Dry GRI permeability (m ²)	Dry GRI permeability (nd)
2	2.50	2.47	2.62	5.9	9.83×10^{-20}	99.6
6	2.52	2.50	2.63	4.9	3.58×10^{-20}	36.3

^a Analyzed by Weatherford Ltd. As-received bulk volume and bulk densities are determined on intact bulk sample material. Bulk material was crushed to yield less than 3.2-mm-sized material, and all other analyses above were conducted on the crushed material. In a vacuum oven set at 212 °F, 85 g of as-received state crushed material is dried. Sample weights are monitored daily until weight stabilization is achieved (± 0.01 g). The dried grain volume of each sample is measured by helium injection using the Boyle’s law method. The sample is subjected to a gas permeability determination using a pressure decay method by Luffel et al. (1993)

Table 6 Measured gas permeabilities values corrected for the Klinkenberg’s slippage effect

Sample	P_c (MPa)	P_p (MPa)	k_a (m ²)	k_a (nd)	b_k^a (MPa)	$1 + \frac{b_k}{P_p}$	k_∞^b (m ²)	k_∞ (nd)
2V	10.4	6.7	2.3×10^{-21}	2.53	12.3	2.8	8.2×10^{-22}	0.8
	17.3	6.8	2.0×10^{-21}	2.33	12.9	2.9	7.0×10^{-22}	0.7
	27.7	6.8	1.3×10^{-21}	1.32	16.1	3.4	3.4×10^{-22}	0.3
	41.5	6.8	5.4×10^{-22}	0.51	21.7	4.2	1.3×10^{-22}	0.1
6H1	10.3	6.9	9.5×10^{-20}	98.08	2.9	1.4	6.7×10^{-20}	67.8
	17.2	6.9	6.5×10^{-20}	68.70	3.3	1.5	4.4×10^{-20}	44.5
	27.6	6.9	3.7×10^{-20}	40.12	4.2	1.6	2.3×10^{-20}	23.0
	41.3	6.9	2.1×10^{-20}	22.29	5.2	1.8	1.2×10^{-20}	11.8
Core 2 GRI	–	0.7	9.8×10^{-20}	99.6	2.8	5.1	1.9×10^{-20}	19.7
Core 6 GRI	–	0.7	3.6×10^{-20}	36.3	4.2	7.1	5.1×10^{-21}	5.2

^a $b_k = 0.11 (k_\infty)^{-0.39}$ Units: b_k (Pa), k_∞ (m²) (Heid et al. 1950)

^b $k_a = k_\infty \left(1 + \frac{b_k}{P_p}\right)$ (Klinkenberg 1941)

to the equivalent liquid permeability k_∞ , average pore pressure P_p , and the Klinkenberg’s gas slippage factor b_k . The correction factor in the parenthesis increases with decreasing gas pressure. Using this approach, we estimate equivalent liquid vertical permeability of $\sim 8.2 \times 10^{-22} \text{m}^2$ (0.8 nd) and equivalent liquid horizontal permeability of $\sim 6.7 \times 10^{-20} \text{m}^2$ (67.8 nd) at 3.5MPa effective stress in two Barnett Shale samples. The equivalent liquid permeability using GRI data for core 2 is $1.9 \times 10^{-20} \text{m}^2$ (19.7 nd) and for core 6 is $\sim 5.1 \times 10^{-21} \text{m}^2$ (5.2 nd). These values are consistent with the horizontal permeability values 6.7×10^{-20} (67.8 nd) to $1.2 \times 10^{-20} \text{m}^2$ (11.8 nd) but much higher than the vertical permeability values 8.2×10^{-22} (0.8 nd) to $1.3 \times 10^{-22} \text{m}^2$ (0.1 nd) (Table 6; Fig. 8). This result is due to the three-dimensional flow condition set on crushed particles in the GRI method as compared to the one-dimensional flow condition set on the sample in the pulse-decay testing.

Our results suggest that quality sample preparation and visual inspection of plug integrity using μ -CT images are critical first steps to obtain reliable permeability measurements on core plugs. When the reservoir volumes are comparable to pore volume of the sample, the pulse-decay technique can also be used to identify fractures not identified in μ -CT. The GRI permeability is often reported at two to three orders of magnitude lower than core-plug

scale pulse-decay permeability (Handwerger et al. 2011; Suarez-Rivera et al. 2012; Tinni et al. 2012). For example, Heller et al. (2014) reported GRI permeability for Barnett 31 and Barnett 27 of 5–14 nd, compared to pulse-decay permeability of 160 nd and $1 \mu\text{d}$, respectively. Handwerger et al. (2011) found that pulse-decay permeability stabilizes to GRI permeability at high confining pressures, arguing that shales are likely to develop microfractures along bedding planes during coring and core extraction.

5.2 Stress Dependence of Horizontal and Vertical Permeability Values

In this study, we observe a fivefold decrease in permeability when the effective stress is increased from 3.5 to 35.0 MPa. Vertical permeability decreases from 2.3×10^{-21} to $5.4 \times 10^{-22} \text{m}^2$, and horizontal permeability decreases from 9.5×10^{-20} to $2.1 \times 10^{-20} \text{m}^2$ (Fig. 6). The pressure-sensitivity factors α of both samples in this study are $0.0435 \text{ (MPa}^{-1}\text{)}$. This value is consistent with pressure-sensitivity factors calculated using the permeability-versus-stress data given in the literature for the Barnett Shale.

Using $k = k_0 \exp(-\alpha(P_c - P_p))$, at similar effective stresses for horizontal samples, pressure-sensitivity factors are 0.0580 and $0.0435 \text{ (MPa}^{-1}\text{)}$ from Kang et al. (2011) (samples 21 and 23, respectively), and 0.0290 and $0.0435 \text{ (MPa}^{-1}\text{)}$ from Vermylon (2011) (samples 31 and 27, respectively). The pressure-sensitivity factor for the Bustin et al. (2008) Barnett sample is $0.1305 \text{ (MPa}^{-1}\text{)}$, which is three times higher than the values above. Since poor-quality (fractured) samples can yield apparently high permeability and elevated-stress sensitivity, we emphasize the importance of sample-integrity testing using high-resolution $\mu\text{-CT}$ images prior to permeability testing, and thoughtful selection of reservoir size in the pulse-decay apparatus in order to illuminate sample heterogeneities [for example, Kamath et al. (1992)]. Information on stress dependence is important for predicting and modeling permeability (Armitage et al. 2011).

We found that both the horizontal and vertical permeability are equally sensitive to stress. In general, the horizontal permeability is expected to be more sensitive to stress than the vertical permeability. The higher stress sensitivity of horizontal permeability is usually attributed to the presence of crack-like voids parallel to bedding due to sample disturbance and their closure upon loading (Kwon et al. 2004). Mckernan et al. (2014) found identical stress sensitivity of horizontal and vertical permeability only after repeated cycles of compression and decompression. Depending on the sample quality, it is therefore possible that part of the stress dependence observed in the laboratory is simply due to reversing the core damage resulted from stress relief and gas expansion experienced by the core during the retrieval process from the subsurface, core plugging operation, and desiccation during sample preparation process. The applied stress could be reversing the core damage by closing the microfractures resulting in lower permeability. Chalmers et al. (2012) and Ghanizadeh et al. (2014a) infer that the stress sensitivity of permeability in shales is primarily controlled by the mineralogy and the nature of pore systems.

5.3 Permeability Anisotropy

We show that horizontal permeability is $\sim 40\times$ higher than vertical permeability at 3.55 MPa effective stress (Fig. 5) persisting up to 35 MPa (Fig. 6). This permeability anisotropy behavior observed in the Barnett Shale is consistent with the Muskwa and Besa River Formation samples from northeastern British Columbia, Canada, measured by Chalmers et al. (2012). However, Ghanizadeh et al. (2014a) for Posidonia Shale (Lower Toarcian, Germany) and Pathi (2008) for Western Canadian and Woodford Shales reported permeability anisotropy

~ 1000 or higher. [Kwon et al. \(2004\)](#) found a much lower-permeability anisotropy of ~ 10 at effective stresses comparable to ours (~ 3 MPa) but approached to unity at effective stresses greater than 10 MPa due to higher stress sensitivity of the horizontal permeability attributed to the presence of crack-like voids parallel to bedding and their closure upon loading. [Metwally and Sondergeld \(2011\)](#) found permeability anisotropy ranging from 3 to 5 in gas shales.

We believe that high- and low-permeability interbeds cause the elevated permeability anisotropy in our Barnett Shale samples. The internal subfacies architecture and microstructure present in the core plugs are revealed by the μ -CT and SEM images analysis (Figs. 1, 2).

Figure 2b clearly shows preferentially horizontal alignment of clay-rich fabric. In Fig. 1c, based on density variation from the μ -CT image, ~ 4 –8-mm stratigraphic layering is evident. Furthermore, by a point-counting method on high-magnification SEM images of the prepared thin sections, we find that dark layers contain $\sim 4\%$ organic matter while light layers contain $\sim 1\%$ (Fig. 1c). Since a majority of the pore space is in the organic matter for Barnett Shale ([Loucks et al. 2009](#); [Curtis et al. 2012](#); [Loucks et al. 2012](#); [Milliken et al. 2012](#)), we believe that the dark layers have higher permeability.

Our result agrees with earlier studies—high anisotropy in mudrocks should be attributed to heterogeneities such as stratigraphic layering ([Witt and Brauns 1983](#); [Clennell et al. 1999](#); [Yang and Aplin 2007](#); [Armitage et al. 2011](#); [Daigle and Dugan 2011](#); [Vega et al. 2014](#)). Permeability anisotropy of < 3 has been extensively reported in natural and synthetic mudrocks ([Clennell et al. 1999](#); [Adams et al. 2013](#)); it is attributed to fabric anisotropy driven by the preferential orientation of platy clay particles. [Armitage et al. \(2011\)](#) argue that simple tortuosity models alone are insufficient to explain higher permeability anisotropy observed in natural rocks that have undergone processes such as cementation or growth of authigenic clays in already narrow pore throats.

6 Conclusions

1. We document vertical permeability of $\sim 2.3 \times 10^{-21} \text{m}^2$ (2.3 nd) and horizontal permeability of $\sim 9.5 \times 10^{-20} \text{m}^2$ (98.1 nd) at 3.5 MPa effective stress in two Barnett Shale samples.
2. The vertical permeability decreases from 2.3×10^{-21} to $5.4 \times 10^{-21} \text{m}^2$ and the horizontal permeability decreases from 9.5×10^{-20} to $2.1 \times 10^{-20} \text{m}^2$ when the effective stress is increased from 3.5 to 35.0 MPa. We infer this stress dependence is due to pore closure and increase in flow-path tortuosity.
3. We show permeability anisotropy, the ratio of the horizontal to the vertical permeability, of ~ 40 in the Barnett Shale. The permeability anisotropy does not vary as a function of effective stress. We infer that the permeability anisotropy is due to the stratigraphic layering in the Barnett Shale.
4. We find that the GRI permeability values are consistent with the horizontal permeability but much higher than the vertical permeability.
5. We infer that the multiscale permeability observed is due to millimeter-scale interbeds of more permeable, organic-rich material with less permeable, more siliceous material.
6. We quantify stress dependence and characterize an anisotropic model to describe the matrix permeability behavior of the Barnett Shale. These results can be used to constrain material behavior in reservoir simulation.

Acknowledgments This research project is funded by Shell under the Shell–UT Unconventional Research (SUTUR) program. We thank Julia Reece for her help during the early stages of this research, Patrick Smith for taking the backscattered electron images, and Jessica Maisano for taking the microscale X-ray computed tomography images. Publication authorized by the Director of the Bureau of Economic Geology, The University of Texas at Austin™.

References

- Adams, A.L., Germaine, J.T., Flemings, P.B., Day-Stirrat, R.J.: Stress induced permeability anisotropy of resedimented Boston Blue Clay. *Water Resour. Res.* **49**, 1–11 (2013). doi:[10.1002/wrcr.20470](https://doi.org/10.1002/wrcr.20470)
- Armitage, P.J., Faulkner, D.R., Worden, R.H., Aplin, A.C., Butcher, A.R., Iliffe, J.: Experimental measurement of, and controls on, permeability and permeability anisotropy of caprocks from the CO₂ storage project at the Krechba Field, Algeria. *J. Geophys. Res. Solid Earth* **116**, B12208 (2011). doi:[10.1029/2011JB008385](https://doi.org/10.1029/2011JB008385)
- Best, M.E., Katsube, T.J.: Shale permeability and its significance in hydrocarbon exploration. *Lead. Edge* **14**, 165–170 (1995)
- Brace, W.F., Walsh, J.B., Frangos, W.T.: Permeability of granite under high pressure. *J. Geophys. Res.* **73**(6), 2225–2236 (1968). doi:[10.1029/JB073i006p02225](https://doi.org/10.1029/JB073i006p02225)
- Bustin, A.M., Bustin, R.M.: Importance of rock properties on the producibility of gas shales. *Int. J. Coal Geol.* **103**, 132–147 (2012). doi:[10.1016/j.coal.2012.04.012](https://doi.org/10.1016/j.coal.2012.04.012)
- Bustin, A.M., Cui, X., Ross, D.J.K., Pathi, V.S.M.: Impact of shale properties on pore structure and storage characteristics. SPE paper 119892 presented at the SPE Shale Gas Production Conference held in Fort Worth, Texas, 16–18 November 2008. doi:[10.2118/119892-MS](https://doi.org/10.2118/119892-MS)
- Chalmers, G.R.L., Ross, D.J.K., Bustin, R.M.: Geological controls on matrix permeability of Devonian gas shales in the Horn River and Liard basins, northeastern British Columbia, Canada. *Int. J. Coal Geol.* **103**, 120–131 (2012). doi:[10.1016/j.coal.2012.05.006](https://doi.org/10.1016/j.coal.2012.05.006)
- Clarkson, C.R.: Production data analysis of unconventional gas wells: review of theory and best practices. *Int. J. Coal Geol.* **109–110**, 101–146 (2013). doi:[10.1016/j.coal.2013.01.002](https://doi.org/10.1016/j.coal.2013.01.002)
- Clarkson, C.R., Nobakht, M., Kaviani, D., Ertekin, T.: Production analysis of tight-gas and shale-gas reservoirs using the dynamic-slippage concept. *SPE J.* **17**(1), 230–242 (2012)
- Clennell, M.B., Dewhurst, D.N., Brown, K.M., Westbrook, G.K.: Permeability anisotropy of consolidated clays. *Geol. Soc. Lond. Spec. Publ.* **158**(1), 79–96 (1999). doi:[10.1144/gsl.sp.1999.158.01.07](https://doi.org/10.1144/gsl.sp.1999.158.01.07)
- Comisky, J.T., Santiago, M., McCollom, B., Buddhala, A., Newsham, K. E.: Sample size effects on the application of Mercury Intrusion Capillary Pressure for determining the storage capacity of tight gas and oil shales. CSUG/SPE paper 149432 presented at the Canadian Unconventional Resources Conference held in Calgary, Alberta, 15–17 November 2011. doi:[10.2118/149432-MS](https://doi.org/10.2118/149432-MS)
- Cui, X., Bustin, A.M.M., Bustin, R.M.: Measurements of gas permeability and diffusivity of tight reservoir rocks: different approaches and their applications. *Geofluids* **9**(3), 208–223 (2009). doi:[10.1111/j.1468-8123.2009.00244.x](https://doi.org/10.1111/j.1468-8123.2009.00244.x)
- Curtis, M.E., Sondergeld, C.H., Ambrose, R.J., Rai, C.S.: Microstructural investigation of gas shales in two and three dimensions using nanometer-scale resolution imaging. *AAPG Bull.* **96**(4), 665–677 (2012). doi:[10.1306/08151110188](https://doi.org/10.1306/08151110188)
- Daigle, H., Dugan, B.: Permeability anisotropy and fabric development: a mechanistic explanation. *Water Resour. Res.* **47**(12), W12517 (2011). doi:[10.1029/2011WR011110](https://doi.org/10.1029/2011WR011110)
- Dicker, A.I., Smits, R.M.: A practical method for determining permeability from laboratory pressure-pulse decay measurements. SPE paper 17578 presented at the International Meeting on Petroleum Engineering held in Tianjin, China, 1–4 November 1988
- EIA (U.S. Energy Information Administration): Technically recoverable shale oil and shale gas resources: An assessment of 137 shale formations in 41 countries outside the United States, pp. 730 (2013)
- Gale, J., Holder, J.: Natural fractures in some U.S. shales and their importance for gas production. Geological Society of London, Petroleum Geology Conference, Series 7, 1131–1140 (2010). doi:[10.1144/0071131](https://doi.org/10.1144/0071131)
- Gale, J., Reed, R.M., Holder, J.: Natural fractures in the Barnett Shale and their importance for hydraulic fracture treatments. *AAPG Bull.* **91**(4), 603–622 (2007). doi:[10.1306/110106060601](https://doi.org/10.1306/110106060601)
- Ghanizadeh, A., Gasparik, M., Amann-Hildenbrand, A., Gensterblum, Y., Krooss, B.M.: Experimental study of fluid transport processes in the matrix system of the European organic-rich shales: I. Scandinavian alum shale. *Mar. Pet. Geol.* **51**, 79–99 (2014a). doi:[10.1016/j.marpetgeo.2013.10.013](https://doi.org/10.1016/j.marpetgeo.2013.10.013)
- Ghanizadeh, A., Amann-Hildenbrand, A., Gasparik, M., Gensterblum, Y., Krooss, B.M., Littke, R.: Experimental study of fluid transport processes in the matrix system of the European organic-rich shales: II.

- Posidonia Shale (Lower Toarcian, northern Germany). *Int. J. Coal Geol.* **123**, 20–33 (2014b). doi:[10.1016/j.coal.2013.06.009](https://doi.org/10.1016/j.coal.2013.06.009)
- Handwerker, D.A., Keller, J., Vaughn, K.: Improved petrophysical core measurements on tight shale reservoirs using retort and crushed samples. SPE paper 47456 presented at the SPE Annual Technical Conference and Exhibition held in Denver, Colorado, USA, 30 October–2 November 2011. doi:[10.2118/147456-MS](https://doi.org/10.2118/147456-MS)
- Heid, J.G., McMahon, J.J., Nielsen, R.F., Yuster, S.T.: *Study of the Permeability of Rocks to Homogenous Fluids*, pp. 230–246. API Drilling & Production Practice, New York (1950)
- Heller, R.: *Multiscale Investigation of Fluid Transport in Gas Shales*. PhD Thesis, Stanford University, Palo Alto, California, USA, pp. 182 (2013)
- Heller, R., Vermynen, J., Zoback, M.: Experimental investigation of matrix permeability of gas shales. *AAPG Bull.* **98**(5), 975–995 (2014). doi:[10.1306/09231313023](https://doi.org/10.1306/09231313023)
- Hickey, J.J., Henk, B.: Lithofacies summary of the Mississippian Barnett Shale, Mitchell 2 T.P. Sims well, Wise County, Texas. *AAPG Bull.* **91**(4), 437–443 (2007). doi:[10.1306/12040606053](https://doi.org/10.1306/12040606053)
- Hinkley, R., Gu, Z., Wong, T., Camilleri, D.: Multi-porosity simulation of unconventional reservoirs. SPE 167146 paper presented at the SPE Unconventional Resources Conference Canada held in Calgary, Alberta, Canada, 5–7 November 2013. doi:[10.2118/167146-MS](https://doi.org/10.2118/167146-MS)
- Hsieh, P.A., Tracy, J.V., Neuzil, C.E., Bredehoeft, J.D., Silliman, S.E.: A transient laboratory method for determining the hydraulic properties of tight rocks. 1. Theory. *Int. J. Rock Mech. Min. Sci.* **18**(3), 245–252 (1981). doi:[10.1016/0148-9062\(81\)90979-7](https://doi.org/10.1016/0148-9062(81)90979-7)
- Jones, S.C.: A technique for faster pulse-decay permeability measurements in tight rocks. *SPE Form. Eval.* **12**(1), 19–26 (1997). doi:[10.2118/28450-PA](https://doi.org/10.2118/28450-PA). SPE 28450
- Jones, F.O., Owens, W.W.: A laboratory study of low permeability gas sands. SPE 7551. In: Presented at the 1979 SPE Symposium on Low-Permeability Gas Reservoirs, Denver, May 20–22 (1979)
- Kamath, J., Boyer, R.E., Nakagawa, F.M.: Characterization of core-scale heterogeneities using laboratory pressure transients. *SPE Form. Eval.* **7**(3), 219–227 (1992). SPE 20575
- Kang, S.M., Fathi, E., Ambrose, R.J., Akkutlu, I.Y., Sigal, R.F.: Carbon dioxide storage capacity of organic-rich shales. *SPE J.* **16**(4), 842–855 (2011). doi:[10.2118/134583-PA](https://doi.org/10.2118/134583-PA). SPE 134583
- Klinkenberg, L.J.: The permeability of porous media to liquids and gases. Paper presented at the API 11th mid year meeting, Tulsa, Oklahoma, May 1941; in *Drilling and Production Practice*, pp. 200–213 (1941)
- Kwon, O., Kronenberg, A.K., Gangi, A.F., Johnson, B., Herbert, B.E.: Permeability of illite-bearing shale: 1. Anisotropy and effects of clay content and loading. *J. Geophys. Res.* **109**, B10205 (2004). doi:[10.1029/2004jb003052](https://doi.org/10.1029/2004jb003052)
- Loucks, R.G., Reed, R.M., Ruppel, S.C., Hammes, U.: Spectrum of pore types and networks in mudrocks and a descriptive classification for matrix-related mudrock pores. *AAPG Bull.* **96**(6), 1071–1098 (2012). doi:[10.1306/08171111061](https://doi.org/10.1306/08171111061)
- Loucks, R.G., Reed, R.M., Ruppel, S.C., Jarvie, D.M.: Morphology, genesis, and distribution of nanometer scale pores in siliceous mudstones of the Mississippian Barnett shale. *J. Sediment. Res.* **79**(12), 848–861 (2009)
- Loucks, R.G., Ruppel, S.C.: Mississippian Barnett Shale: Lithofacies and depositional setting of a deep-water shale gas succession in the Fort Worth Basin, Texas. *AAPG Bull.* **91**(4), 579–601 (2007)
- Luffel, D.L., Hopkins, C.W., Holditch, S.A., Schetter, P.D.: Matrix permeability measurement of gas productive shales. SPE Annual Technical Conference and Exhibition, Houston, Texas. SPE 26633, 261–270 (1993). doi:[10.2118/26633-MS](https://doi.org/10.2118/26633-MS)
- Mckernan, R.E., Rutter, E.H., Mecklenburgh, J., Taylor, K.G., Covey-Crump, S.J.: Influence of effective pressure on mudstone matrix permeability: implications for shale gas production. SPE paper 167762 presented at the SPE/EAGE European Unconventional Conference and Exhibition held in Vienna, Austria, 25–27 February 2014
- Metwally, Y.M., Sondergeld, C.H.: Measuring low permeabilities of gas-sands and shales using a pressure transmission technique. *Int. J. Rock Mech. Min. Sci.* **48**(7), 1135–1144 (2011). doi:[10.1016/j.ijrmm.2011.08.004](https://doi.org/10.1016/j.ijrmm.2011.08.004)
- Milliken, K.L., Esch, W.L., Reed, R.M., Zhang, T.W.: Grain assemblages and strong diagenetic overprinting in siliceous mudrocks, Barnett Shale (Mississippian), Fort Worth Basin, Texas. *AAPG Bull.* **96**(8), 1553–1578 (2012). doi:[10.1306/12011111129](https://doi.org/10.1306/12011111129)
- Ning, X.: *The Measurement of Matrix and Fracture Properties in Naturally Fractured Low Permeability Cores using a Pressure Pulse Method*. PhD Thesis, Texas A&M University, College Station, Texas, USA, pp. 204 (1992)
- Ning, X., Fan, J., Holditch, S.A., Lee, W.J.: The measurement of matrix and fracture properties in naturally fractured cores. SPE paper 25898 presented at the Low Permeability Reservoirs Symposium held in Denver, Colorado, 26–28 April 1993. doi:[10.2118/25898-MS](https://doi.org/10.2118/25898-MS)
- NIST (National Institute of Standards and Technology) <http://webbook.nist.gov/chemistry/fluid/> (2014)

- Pathi, V.S.M.: Factors Affecting the Permeability of Gas Shales. Master's Thesis, University of British Columbia, Vancouver, Canada, pp. 189 (2008)
- Patzek, T.W., Male, F., Marder, M.: Gas production in the Barnett Shale obeys a simple scaling theory. *Proc. Natl. Acad. Sci.* **110**(49), 19731–19736 (2013). doi:[10.1073/pnas.1313380110](https://doi.org/10.1073/pnas.1313380110)
- Silin, D.B., Kneafsey, T.J.: Gas shale: from nanometer-scale observations to well modeling. SPE paper 149489 presented at the Canadian Unconventional Resources Conference held in Alberta, Canada, 15–17 November 2011. doi:[10.2118/149489-MS](https://doi.org/10.2118/149489-MS)
- Soeder, D.J.: Porosity and permeability of Eastern Devonian gas shale. *SPE Form. Eval.* **3**(1), 116–124 (1988). doi:[10.2118/15213-PA](https://doi.org/10.2118/15213-PA). SPE Paper 15213
- Stegent, N.A., Ingram, S.R., Callard, J.G.: Hydraulic fracture stimulation design considerations and production analysis. SPE paper 139981 presented at the SPE Hydraulic Fracturing Technology Conference held in The Woodlands, Texas, USA, 24–26 January 2011. doi:[10.2118/139981-MS](https://doi.org/10.2118/139981-MS)
- Suarez-Rivera, R., Chertov, M., Willberg, D.M., Green, S.J., Keller, J.: Understanding permeability measurements in tight shales promotes enhanced determination of reservoir quality. SPE paper 162816 presented at the SPE Canadian Unconventional Resources Conference held in Calgary, Alberta, Canada, 30 October–1 November 2012. doi:[10.2118/162816-MS](https://doi.org/10.2118/162816-MS)
- Tinni, A., Fathi, E., Agarwal, R., Sondergeld, C., Akkutlu, Y., Rai, C.: Shale permeability measurements on plugs and crushed samples. SPE paper 162235 presented at the SPE Canadian Unconventional Resources Conference held in Calgary, Alberta, Canada, 30 October–1 November 2012. doi:[10.2118/162235-MS](https://doi.org/10.2118/162235-MS)
- Vega, B., Dutta, A., Kovscek, A.: CT imaging of low-permeability, dual-porosity systems using high X-ray contrast gas. *Transp. Porous Med.* **101**, 81–97 (2014). doi:[10.1007/s11242-013-0232-0](https://doi.org/10.1007/s11242-013-0232-0)
- Vermilyen, J.P.: Geomechanical Studies of the Barnett Shale, Texas, USA. PhD Thesis, Stanford University, Palo Alto, California, pp. 143 (2011)
- Waters, G.A., Dean, B.K., Downie, R.C., Kerrihard, K.J., Austbo, L., McPherson, B.: Simultaneous hydraulic fracturing of adjacent horizontal wells in the Woodford Shale. SPE paper 119635 presented at the SPE Hydraulic Fracturing Technology Conference held in The Woodlands, Texas, 19–21 January 2009. doi:[10.2118/119635-MS](https://doi.org/10.2118/119635-MS)
- Witt, K.-J., Brauns, J.: Permeability–anisotropy due to particle shape. *J. Geotech. Eng.* **109**(9), 1181–1187 (1983)
- Yang, Y.L., Aplin, A.C.: Permeability and petrophysical properties of 30 natural mudstones. *J. Geophys. Res. Solid Earth* **112**, B03206 (2007). doi:[10.1029/2005JB004243](https://doi.org/10.1029/2005JB004243)
- Ziarani, A.S., Aguilera, R.: Knudsen's permeability correction for tight porous media. *Transp. Porous Med.* **91**, 239–260 (2012). doi:[10.1007/s11242-011-9842-6](https://doi.org/10.1007/s11242-011-9842-6)